Dynamics of oceanic slab tearing during transform-fault oblique subduction: Insights from 3D numerical modeling

Jie Xin[1], Huai Zhang[1,*], Zhong-Hai Li[1], Felipe Orellana-Rovirosa[2], Liang Liu[3], Yigang Xu[3], Zhen Zhang[1], Yaolin Shi[1]

[1]Key Laboratory of Computational Geodynamics, College of Earth and Planetary Sciences, University of Chinese Academy of Sciences, Beijing 100049, China

[2]Department of Ocean Science and Engineering, Southern University of Science and Technology, Shenzhen 518055, China

[3]State Key Laboratory of Isotope Geochemistry, Guangzhou Institute of Geochemistry, Chinese Academy of Sciences, Guangzhou 510640, China

Key Points:

- 3-D numerical models are conducted to study the mechanism of oceanic slab vertical tearing under transform-fault oblique subduction.
- The horizontal obliqueness and slab transform age-difference play dominant roles in determining the style of vertical slab tearing.
- The continual variation in dip angle observed along a trench could be related to plate oblique convergence and a possible slab tearing.

Abstract

Oceanic slab vertical tearing is prevalently identified in the present Earth. More general background for vertical slab tearing is the transform-fault subduction during horizontally-oblique tectonic convergence. However, its geodynamic mechanisms are poorly understood to date. This work introduces a full numerical 3-D time-dependent Stokes' thermo-mechanical flow model to investigate the characteristics and mechanism of vertical tearing of active transform-faulted oceanic slab during oblique subduction. We find that (i) transform-fault ages-offset and (ii) subduction horizontal obliqueness have the first-order control, even without the lateral physical-property differences. The overriding plate enforces (surface contact interaction) bending of one slab first, which superimposes the differential sinking driven by slabs-age-thickness differences. For obliqueness angles 30° and/or age-ratios of the secondly-bent to the firstly-bent slab being <0.6, well-developed slab vertical tearing is unavoidable inside the mantle. Quantifying the horizontal distance vector between sinking slabs, we find that young overall lithosphere (average <30 Myr, for any age ratio) at high subduction obliqueness angles (>~25°) tends to produce trench-parallel slab tearing. In contrast, combinations of small-intermediate obliqueness angles (0-30°) and age ratios with the slab that bends at the trench first being relatively older-thicker, tend to produce trench-perpendicular tearing, which is related to differential slabs-hinge retreat or rollback. These numerically-predicted scenarios and phenomena are consistent with plate-tear

imaging results from subduction zones. Our modeling results also suggest that the continual along-trench variation in subduction dip angle may be related to oblique subduction's early stages of evolution.

Keywords: slab's vertical tearing, oblique subduction, transform fault offset, 3D numerical models.

Plain Language Summary

Tectonic plates supporting the oceans can tear-off through time as they plunge and sink into the Earth's mantle and are especially favored when plates have preexisting fault-weak zones. Two primary conditions promote tectonic oceanic-slabs' tearing: (1) Obliqueness of a plate's horizontal velocity with respect to the overriding-plate coastline and trench, as the latter will enforce bending of one side of the slab first causing differences in deformation; (2) Differences in slab age between two sides of a displaced fault-zone that created an offset in plate age and thickness. To understand these processes, we present 3D numerical models that simulate tectonic evolution and deformations, and we compare model results with analytical studies and natural observations from seismic imaging. We find that age differences across fault zones combined with subduction horizontal obliqueness control the generation and development of vertical tearing, and two geometrical patterns of vertical tearing are largely consistent with observations. Our findings suggest that along-trench changes in the vertical angle between slab and surface (dip angle), may be related to early stages of oblique subduction. Observing the age contrast across faults and the horizontal obliqueness of plates' motion allows predictions of the tearing pattern, evolution, and local mantle flow.

1. Introduction

Slab tearing (or break-off) is a general phenomenon on present-day Earth. When occurring, the resulting slab window allows hot mantle materials to pass through, resulting in anomalous thermal and chemical conditions in convergent-margin environments (Gianni & Luján, 2021; Thorkelson, 1996). If slab tearing occurs at shallow depth (Freeburn et al., 2017; Király et al., 2020), the asthenospheric upwelling produces significant geological and geophysical responses, including complex mantle flow in subduction zones (Bolton et al., 2022; R. Govers & Wortel, 2005; Rosenbaum et al., 2008), anomalous thermal and mechanical structures of the overlying plate (Georgieva et al., 2016; Guillaume et al., 2010; Jolivet et al., 2015; Roche et al., 2018), as well as active arc and backarc magmatism (Gianni & Luján, 2021; K. Liu et al., 2020; Xu et al., 2020).

Slab tearing can be categorized into horizontal and vertical tearing patterns (Rosenbaum et al., 2008). The horizontal tearing normally occurs along a sub-horizontal plane, in which the lower segment of the slab detaches from the upper segment and then sinks into the mantle. In this case, the negative buoyancy of the subducted slab contributes to slab break-off (tearing) (Duretz et al., 2011;

Gerya, 2022; Hildebrand et al., 2018; Kufner et al., 2017; L. Liu et al., 2021). On the other hand, it is generally difficult for a coherent subducting slab to tear along sub-vertical planes perpendicular to the trench (Cui & Li, 2022) due to the lack of major forces in the along-strike direction. However, vertical slab tearing occurs in many subduction zones of present-day Earth (Figure 1), including Mariana's subduction zone (M. S. Miller et al., 2004; Meghan S. Miller et al., 2006), the Mediterranean zone (Jolivet et al., 2021; Suckale et al., 2009), Aegean and Anatolia regions (Rob Govers & Fichtner, 2016; Jolivet et al., 2015), Central America zone (Carciumaru et al., 2020; Dougherty & Clayton, 2014; Stubailo et al., 2012; Thorkelson, 1996), South America zone (Pesicek et al., 2012; Rosenbaum et al., 2008; Vargas & Mann, 2013), Caribbean zone (Meighan et al., 2013), Tonga zone (Bonnardot et al., 2009; Millen & Hamburger, 1998), and Kamchatka subduction zone (Levin et al., 2002).

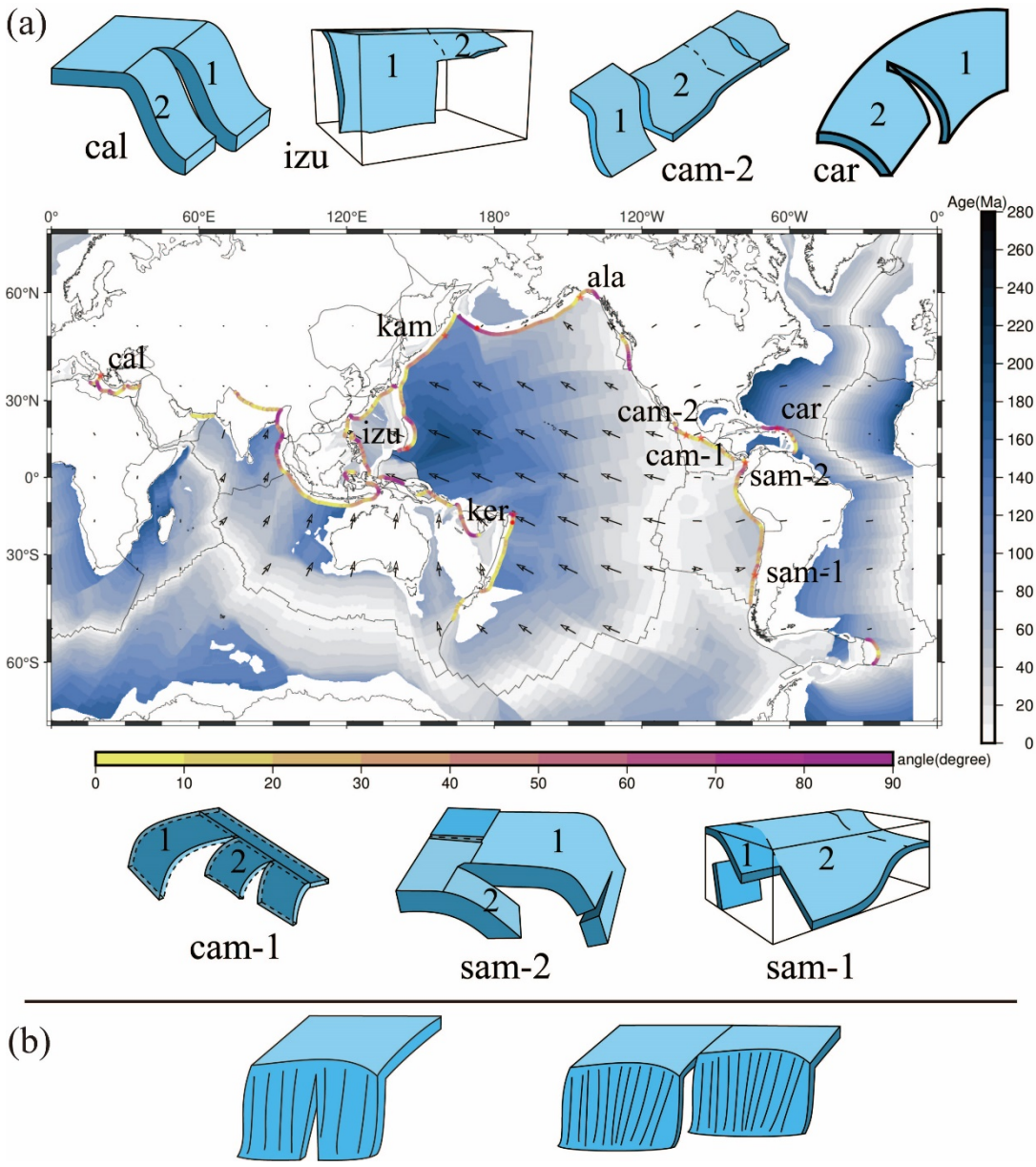

Figure 1. Global distribution of slab tearing in the present-day oceanic subduction zones. (a) The red stars on the map and the cartoons above or below show each case's position and deep structure. The cartoons are shown for '**ala**,' '**kam**,' and '**ker**' due to the lack of relevant data. The references for these subduction zones are: **ker**: Bonnardot et al., 2009; **cam-2**: Carciumaru et al., 2020; Dougherty and Clayton, 2014; **kam**: Levin et al., 2002; **car**: Meighan et al., 2013; **izu**: Miller et al., 2006; **sam-1**: Pesicek et al.,

2012; **cam-1**: Stubailo et al., 2012; **cal**: Suckale et al., 2009; **sam-2**: Vargas and Mann, 2013; **ala**: Yang and Gao, 2020. The identifications of plate-1 and 2 are defined as follows: Plate-1 is the plate that would arrive and contact the trench earlier, whereas Plate-2 would do it later. The vertical color bar represents the age of the oceanic lithosphere, and the horizontal color bar is the angle between horizontal plate velocity and the direction perpendicular to the trench. The arrows indicate the plate velocity in the hot spot reference frame (Becker et al., 2015). The data on the subduction zone, seafloor age, and color bar are referred to (Hayes et al., 2018a), (Müller et al., 2008), and (Crameri, 2021), respectively. (b) Cartoons illustrate the two typical slab vertical tearing patterns (Rosenbaum et al., 2008).

Slab vertically-propagating tearing inside the mantle generally requires along-strike variations, with several mechanisms being proposed: non-uniform roll-back due to lateral temperature and age changes in subducting plates or step faulting at the edges of active margins (Burkett & Billen, 2010; R. Govers & Wortel, 2005), opposite rotation of slab segments (Gianni et al., 2019), the oceanic/continental plate transition (Li et al., 2013), and variable orientations of passive margins (Fernández-García et al., 2019). A more general background for vertical slab tearing is the transform-faulted slab subduction, with contrasting seafloor ages on both sides of a weak fault zone (Burkett & Billen, 2010; Magni et al., 2014; Pusok et al., 2018). In this case, two favorable conditions may facilitate vertical slab tearing, one is the large contrast of slab ages and the other is the oblique subduction of a transform fault. In this study, three-dimensional numerical models are systematically conducted to investigate the mechanism of vertical slab tearing and the causes of different tearing patterns. The model results are further compared with analytical studies as well as natural observations. We also hope this work will provide a profound understanding of inferring the pre-subduction obliqueness angle of a subducted plate that may lack hotspot constraints and improve the accuracy of plate reconstruction.

Table 1. Parameters of the natural subduction zones with slab tearing [a].

Symbol (subduction zone)	Name of the fracture zone	Oblique convergence angle	Age of Plate-1 (t1, Ma)	Age of Plate-2 (t2, Ma)
cam-1 (Central America)	Tehuantepec	°		
cam-2 (Central America)	Orozco	°		
sam-1 (South America)	Mocha	°		

sam-2 (South America)	Caldas slab	°
Izu (Izu-Bonin)	——	°
cal (Calabria)	Central Hellenic Shear Zone	°
car (Caribbean)	——	°
ala (Alaska)	Between the Pacific plate and Yakutat plate	°
kam (Kamchatka-Kuril)	——	°
ker (Kermadec)	Fiji	°

[a] The convergence angle and lithospheric age use the averaged value within 300 km on both sides of the symbol sites on the map (Figure 1).

2. Model setup

The finite-element software ASPECT (version 2.3.0) is used to solve the incompressible Stokes equations (1-2) coupled with temperature advection-diffusion equation (3) velocity $\mathbf{u}$, pressure p, temperature T (Bangerth et al., 2021; Glerum et al., 2018). Equation (4) describes the evolution of additional fields transported along with the velocity field $\mathbf{u}$, without diffusion. For the Stokes' flow equation, we employ the Taylor-Hood spatial element.

$$-\nabla \bullet [2\eta (\varepsilon (\mathbf{u}))] + \nabla p = \rho \mathbf{g} \#(1)$$

$$\nabla \bullet \mathbf{u} = 0 \#(2)$$

$$\rho C_p \left(\frac{\partial T}{\partial t} + \mathbf{u} \bullet \nabla T \right) - \nabla \bullet k \nabla T = 0 \#(3)$$

$$\frac{\partial c_i}{\partial t} + \mathbf{u} \bullet \nabla c_i = 0 \#(4)$$

where c_i is the i-th compositional field that tracks chemical compositions, $\varepsilon(\mathbf{u}) = \frac{1}{2}(\nabla\mathbf{u} + \nabla\mathbf{u}^T)$ is strain rate, η is viscosity, ρ is density, $\mathbf{g}$ is gravitational acceleration, C_p is specific isobaric heat capacity, k is thermal conductivity.

A 3D Cartesian model box with spatial dimensions of 2500 km×3000 km×660 km is used. Figure 2 shows the initial model configuration using the compositional fields, including a partially subducted oceanic lithosphere with a transform fault in the middle and a continental lithosphere as the overriding plate (Figure 2a). The subducting oceanic plate is decoupled from the side plates by applying two side faults, as shown in Figure 2b. In contrast to the central plate, no subducting slab is prescribed for the side plates (Figure 2c).

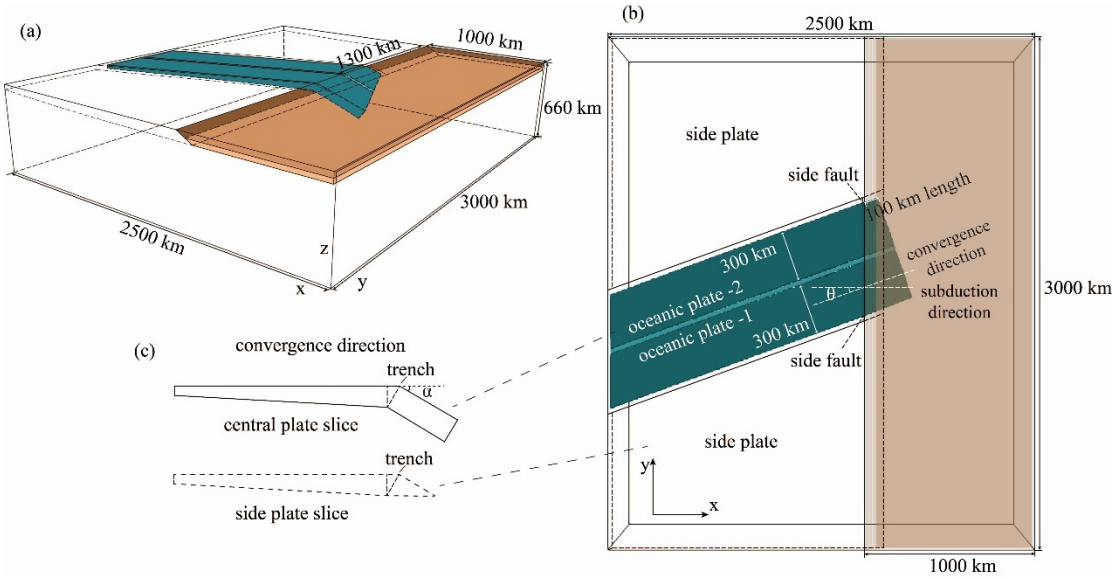

Figure 2. Initial condition model setup. (a) 3D oblique view of the model structure with the subducting (cyan) and overriding (brown) plates. (b) View from above. The oceanic slab's weak central region (transform fault and fault zone) is 30 km wide. (c) The vertical cross-sections on the lateral edges of subducting lithosphere and adjacent plate slice lithosphere. The initial dip angle of the subducting slab is α=30°. The oblique subduction is achieved by rotating the slab with an angle θ. The length of the shortest subducted slab on one side is 100 km and increases gradually to the other side. The axes definition: X-axis is trench-perpendicular, Y-axis is trench-parallel.

The half-space cooling model is used to calculate the ocean plate's initial thermal thickness as $h \approx 2.32\sqrt{\mathrm{t}}$ ($h_{\max} = 100\ km$) (Turcotte & Schubert, 2002), where k is thermal diffusivity, and t is seafloor age. In this sense, the thickness ratio between Plate 1 and 2, *i.e.*, $\frac{h_1}{h_2}$, is dynamically similar to the square root of the ratio of lithospheric ages $\sqrt{\frac{t_1}{t_2}}$. In the mantle domain, an adiabatic

profile is applied as initial condition. The ocean plate's maximum thickness is computationally limited to 100 km, consistent with thermo-rheological observations. The top and bottom boundary temperature is fixed at 293 K and 1700 K, respectively. Except for the fixed (3D zero velocity vector) bottom boundary that is intended to simulate the effect of the 660 km phase-transition interface, the velocity field boundary conditions are of tangential flow boundary (free-slip and no-flow-through) on all the other five surfaces.

Our representation assumes the half-space cooling model with a constant thermal expansion coefficient, under which the plates are defined as a thermal boundary layer specifically limited by two isotherms. The lower boundary deepens with time, thus the plates thicken with age, but their density and viscosity remain constant with well-established values (Table 2). This simplification is only a first-order approximation which allows faster computations. Finally, the computational grid is adaptively refined five times till its smaller element reaches a minimum size of $6.51 \times 6.25 \times 6.88$ km^3. Usually, it takes 24 to 48 hours for each model, running with 220 computing cores, to simulate a geological time of about 30 Myr.

Table 2. Material properties of the numerical models [a].

Compositional units	Density$(kg \bullet m^{-3})$ [b]	Viscosity$(Pa \bullet s)$
Underlying upper mantle	3300	1.4×10^{20}
Oceanic crust	3390	2.8×10^{20}
Oceanic lithospheric mantle	3390	1.4×10^{23}
Continental crust	3350	1.4×10^{24}
Continental lithospheric mantle	3390	1.4×10^{23}
Transform fault zone	3390	7.0×10^{20}
Side fault	3390	7.0×10^{20}
The crust of the side plate	3350	2.8×10^{20}
Lithospheric mantle of the side plate	3390	1.4×10^{23}

[a] Other parameter values: Reference temperature = 293 K; heat capacity = 1250 J/kg/K; thermal conductivity = 2 W/m/K; thermal expansion coefficient = 0.

[b] The value of density implicitly includes the thermal-effect dependence.

3. Results

A total of 69 experiments are conducted with different obliqueness angles and plate ages combinations. To quantify the size of the tear width, we visualized and post-processed the output data in Paraview, specifically by selecting horizontal slices of the oceanic lithosphere at various times and depths and measuring the horizontal vector distance between the two slabs (Figure 3).

3.1. Tested conditions for vertical slab tearing

In our reference model, the slab tearing process can be separated before and after Plate 1 reaches 660 km deep (mapped by oceanic-lithosphere compositional field (in Aspect software) value >0.5 within 15 km from the bottom), as shown by the temperature contour of the reference model (t1=33 Myr t2=27 Myr =20°, Abbreviated as 3327_20, Figure 3).

After Plate 1's tip arrives at the box bottom, its subduction velocity decreases, contributing to the increase of tearing width. The distance at the bottom of the oceanic slabs is determined by whether tearing occurs at a depth larger than 110 km in both stages. As can be seen from the white contour lines (depth: 100-400 km) in Figure 3, vertical tearing can occur at deep locations (>200 km depth). Figure 4 demonstrates the tearing judgments/decision arrays of the experiments.

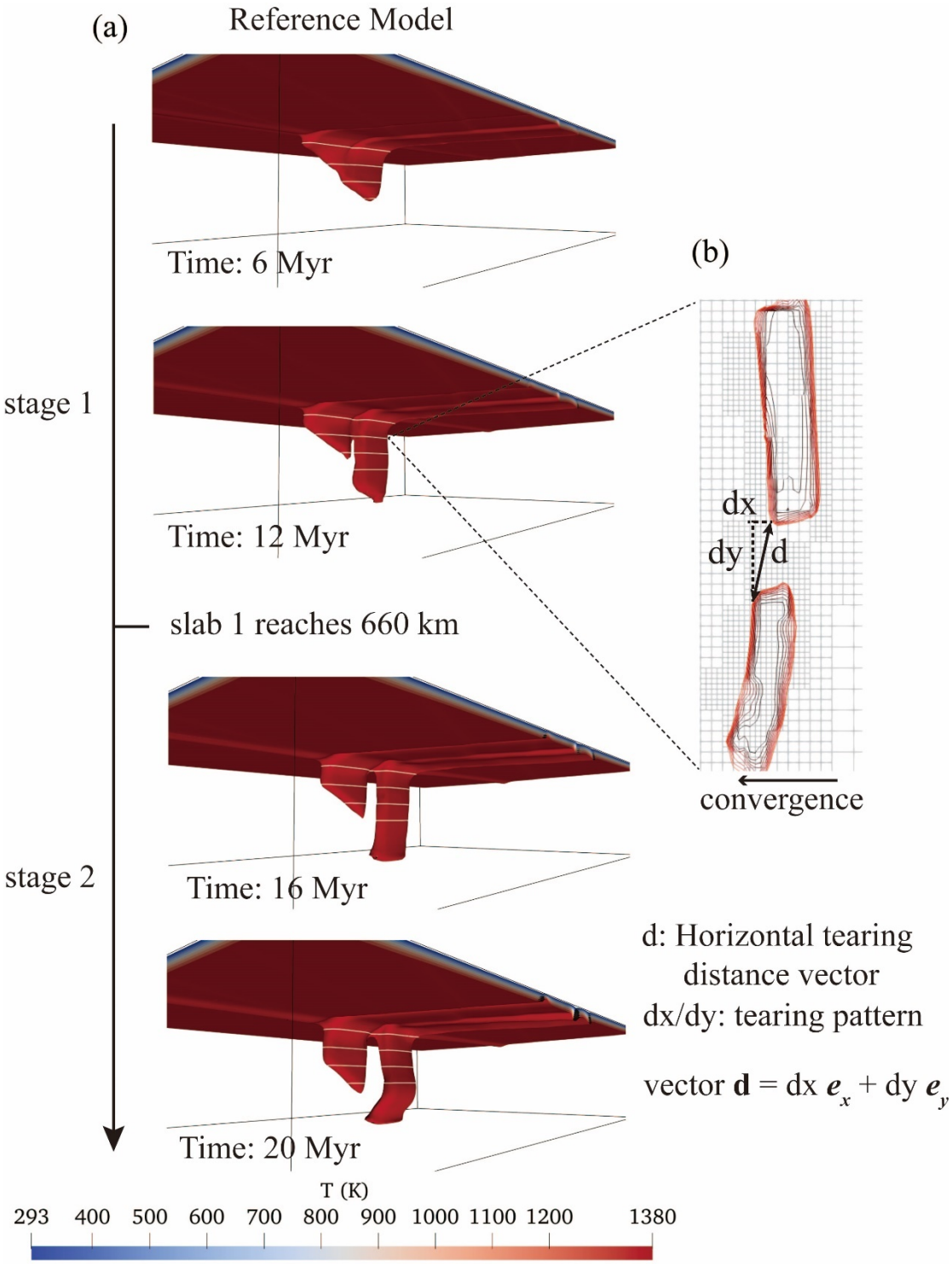
(a)
Reference Model
Time: 6 Myr
(b)
stage 1
Time: 12 Myr
dx
dy
d
slab 1 reaches 660 km
convergence
stage 2
Time: 16 Myr
d: Horizontal tearing distance vector
dx/dy: tearing pattern
vector d = dx e_x + dy e_y
Time: 20 Myr
T (K)
293 400 500 600 700 800 900 1000 1100 1200 1380

Figure 3. (a) Reference model evolution shown by the slab temperature contour of 1380 K (model parameters: lithospheric ages t1 = 33 Ma, t2 = 27 Ma; obliqueness θ=20°). (b) The definition and quantification of slab tearing, with the parameter "d" for the horizontal vector distance (of magnitude 'width') of slab tearing window, and the ratio "dx/dy" indicating/characterizing the slab tearing pattern. If dx/dy < 0.4 for both stages, the pattern is defined as along-trench-strike tearing dominated. In contrast with dx/dy > 0.4 at stage 1 and dx/dy > 0.7 at stage 2, the pattern is defined as trench-strike-perpendicular tearing dominated. On the other hand, if dx/dy > 0.4 at stage 1 but dx/dy $<$ 0.7 at stage 2, it is defined as a transition mode.

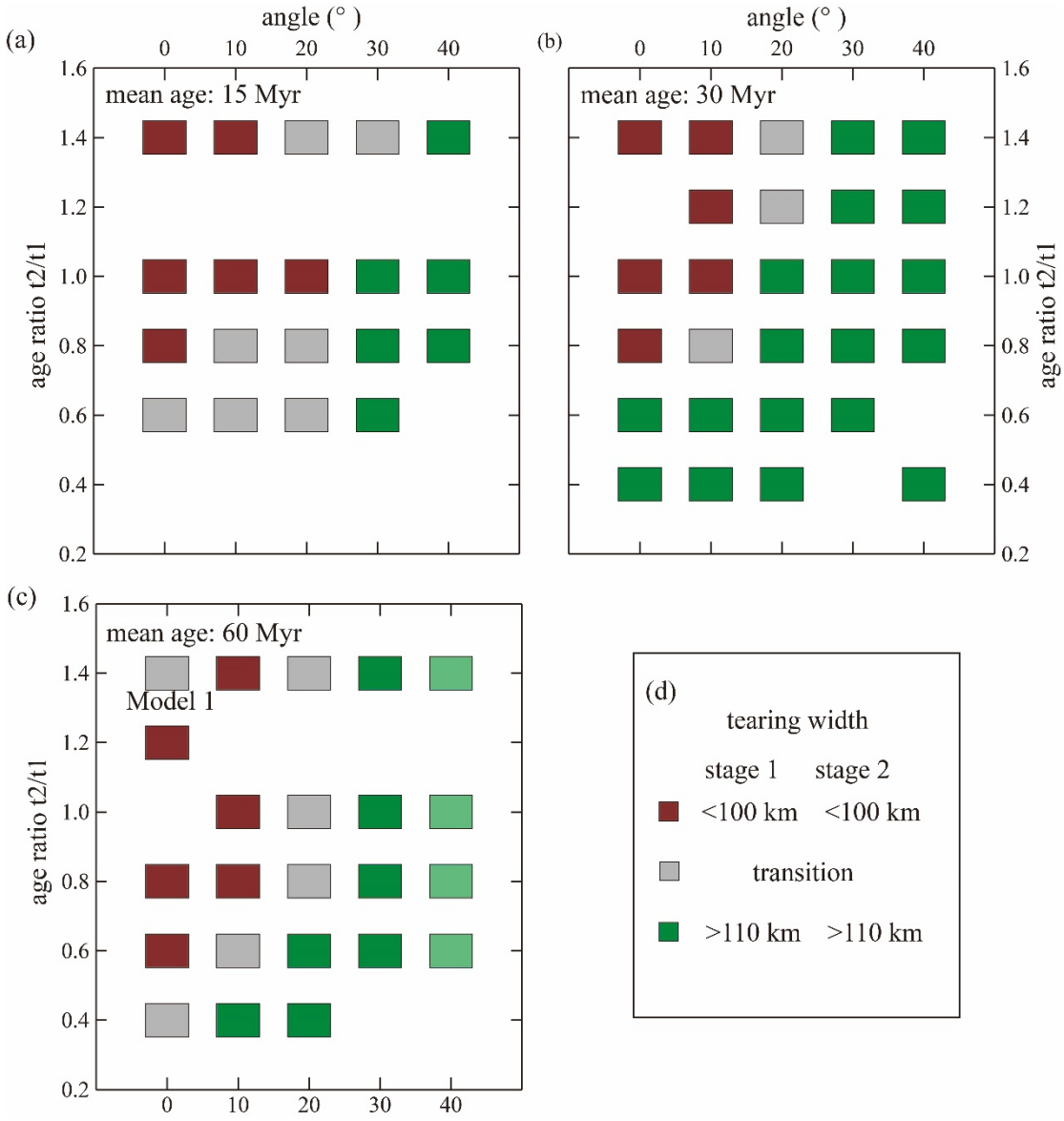

Figure 4. Check-box diagrams for the tested conditions. *Angle* means the obliqueness angles. The mean lithospheric age of plates-1 and 2, ((t1+t2)/2), is 15 Myr (a), 30 Myr (b), and 60 Myr (c), respectively. (d) The category of slab tearing discrimination. If the tearing width is <100 km at both stages, the tearing is classified as absent (red rectangles). In contrast, with slab tearing width >110 km at both stages, the occurrence of slab tearing is affirmatively defined (green rectangles). The cases in between are defined as transitional modes (gray rectangles).

Each diagram in Figure 4 summarizes the results of simulations with the same arithmetic mean age $\frac{t_1+t_2}{2}$ of the plates separated by the transform fault. We use relative age ratio rather than age difference as a way to avoid discussing parameters that deviate far from nature, i.e., $t_1 - t_2 = t_1\left(1 - \frac{t_2}{t_1}\right)$, For the same age ratio, a smaller mean age means a smaller absolute age difference. When the absolute mean age is the same, the slab tearing is favored by a larger obliqueness angle and by older plate-1 ages relative to plate-2. Most models fail to tear without oblique subduction (angle=0) except for medium-aged plates with substantial age differences.

In particular, due to thin slabs, Model 1 (1318_20) in the low mean absolute age group (15 Myr) exhibits lateral break-off, increasing tearing width. The models in the high mean absolute-age group with high horizontal angle (light green area in 60 Myr) would offer plate-1 less vertical subduction distance, limiting tearing propagation at stage 1 but bringing evident tear at stage 2. The simulations in the dark green area demonstrate that oblique convergence can cause major vertical tearing before the plate reaches 660 km and commonly before the large-scale slab differential rollback.

In conclusion, our simulations suggest that for any values of obliquity, the plates tear for age ratios less than 0.6, meaning that an older-thicker plate-1 entering the trench first, sinks first and faster. Furthermore, regardless of the transform age ratio, all the plates tear at obliquities greater than 30°. This latter behavior is likely an effect of the contact surface forces exerted by the overriding (continental) plate on forcing the bending of an obliquely-subducting slab-1 first and then later on slab-2.

3.2. Patterns of vertical slab tearing

In this study, the tearing width at the bottom of the plate is used to indicate whether tearing can occur. In addition, the horizontal tearing width vector and the ratio of its components at about 100 km depth (see Figure 3 for definitions) are employed to characterize the tearing pattern. When dx/dy >0.4 at stage 1 and >0.7 at stage 2, it is defined as trench-perpendicular tearing (related to differential hinge retreat) (Figure 5). In contrast with dx/dy <0.4 for both stages, the pattern is defined as trench-parallel tearing, in which the along-trench-strike tearing dominates. A transitional mode is defined in between.

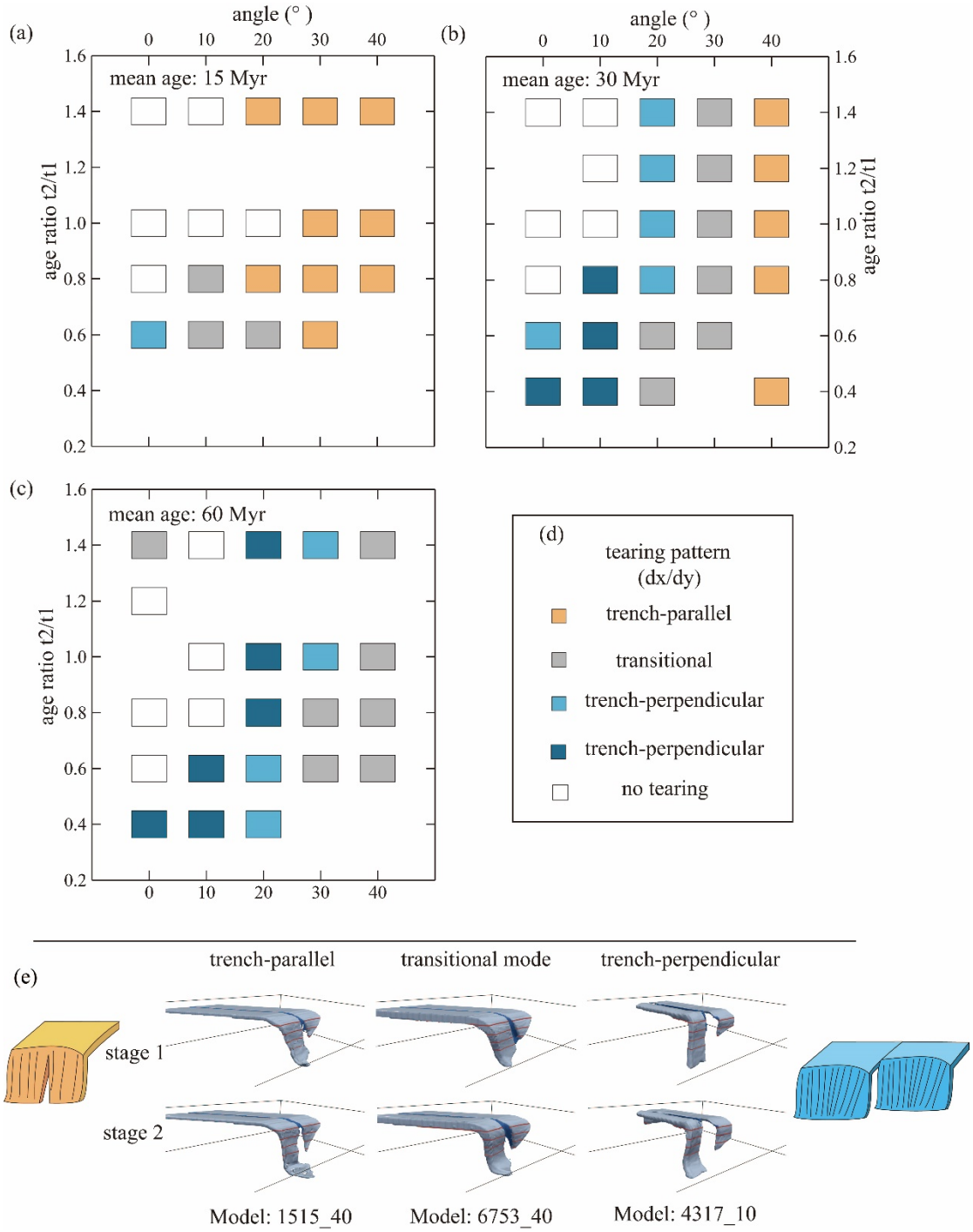

Figure 5. Check-box diagrams for the tearing patterns. *Angle* means

the obliqueness angles. The mean lithospheric age of plates1 and 2, ((t1+t2)/2), is 15 Myr (a), 30 Myr (b), and 60 Myr (c), respectively. (d) The category of slab tearing pattern, depending on the ratio "dx/dy" as shown in Figure 3. If dx/dy < 0.4 for both stages, the pattern is defined as transverse tearing, in which the trench-parallel tearing dominates. In contrast with dx/dy > 0.4 at stage 1 and dx/dy > 0.7 at stage 2, the pattern is defined as dominated by trench-perpendicular tearing. On the other hand, if dx/dy > 0.4 at stage 1 but dx/dy < 0.7 at stage 2, it is defined as a transition mode. (e) Cartoons and typical models illustrate the three different slab tearing patterns.

Plate horizontal obliquity influences the transverse pull-off subparallel to the trench direction. Therefore, high obliqueness angles for same absolute ages favor trench-parallel tearing, while low obliqueness angles favor trench-perpendicular tearing. On the other hand, large absolute age differences generally result in large sinking velocity differences that project in the convergence direction. Thus for obliquities <45°, more trench-perpendicular tearing tends to occur; on the converse, trench-parallel is favored.

4. Discussion

4.1. Analytical study of the slab tearing dynamics

In order to understand how the various governing factors operate and enhance the verifiability of the results, we compare the model results with analytical studies.

We assume that the horizontal width (d) of the tearing window is strongly correlated to the difference in subduction velocity v between the two plates separated by a transform fault. In a 2D subduction model, the oceanic slab is primarily subjected to negative buoyancy $\delta\rho \cdot g \cdot h \cdot l$, surrounding mantle resistance along the tangential direction of the slab $F_1 \sim \eta_1 v$ (where v is the plate speed, η_1 is mantle viscosity), and unbending resistance perpendicular to the slab $F_2 \sim \eta_2 v h^3 / {l_b}^3$, where l_b is the bending length from the slab tip to the unbending place behind the hinge point, η_2 is plate viscosity (Li & Ribe, 2012; Ribe, 2001) (Figure 6c). Then we simply take the tangential velocity $v = \frac{\delta\rho \bullet g}{\eta_1} sin\alpha \cdot h \cdot l$ (in an idealized sinking scenario) along with the slab as the major component of the velocity difference v, yielding

$$v = \frac{\delta\rho \bullet g}{\eta_{\mathrm{mantle}}} (h_1 l_1 - h_2 l_2) \bullet f \#(5)$$

where f is a dimensionless parameter representing the additional effects on v, such as unbending resistance along the slab-normal direction, subduction dip angle, variation of slab bending length over time, viscosity and width of the weak zone, etc.

We assume that in the slab tip of the initial subduction zone, plate thickness h remains constant, yet the initial interface slab length l changes in the trench direction (y-direction) following $l(y, \theta) = \frac{c + y \bullet tan\theta}{\cos}$, where c is fixed at 100 km.

Then we get $v_{3d} = \int_0^w v dy / \int_0^w 1 dy$, as the average velocity of the entire slab tip, with w the horizontal span of the slab.

The velocity difference is obtained as $v_{3d} = k \bullet C \bullet h \bullet f$, where $k = \frac{\delta\rho \bullet g \bullet b \bullet tan\alpha}{2\eta_{\text{mantle}}}$ (the unit is s^{-1}) is a set of dynamic parameters kept constant in this model for the above reasons, and $b = w/cos\theta$ is the fixed plate width.

$$C = 2\frac{c}{b}\left(\sqrt{\frac{t_1}{t_2}} - 1\right) + \left(3\sqrt{\frac{t_1}{t_2}} - 1\right)\frac{\sin}{(\cos)^2}, \#(6)$$

denotes geometry parameters reflecting the oblique subduction effects. $h \approx 2.32\sqrt{\text{t}}$ denotes the plate thickness corresponding to the model's seafloor age.

According to the form $F_2 \sim \eta_2 v h^3 / {l_b}^3$ and dimensionless additional effects parameter f, we use $f \approx \left(\frac{h_2}{h_1}\right)^n \frac{l_{b_1}}{l_{b_2}}$ to indicate the unbending resistance variation difference between two ocean plates.

We used a set of fixed times (10 Myr, 14 Myr, 20 Myr) and depth range (100-400 km) to compare and correlate the tearing width d and the velocity difference v, with the analytical results shown in Figures 6-9. The figures are plotted for different combinations of controlling parameters, e.g., absolute mean ages (15, 30, 60 Myr) and transform-age-contrast combinations. Upon constructing the correlation shown in Figure 6-9 and Table 3, we have removed four data from the simulation, including 1318_30, 1318_40, 1515_20, and 1515_30. Because the over-thin slabs broke off, we can not precisely measure the tearing width in these models.

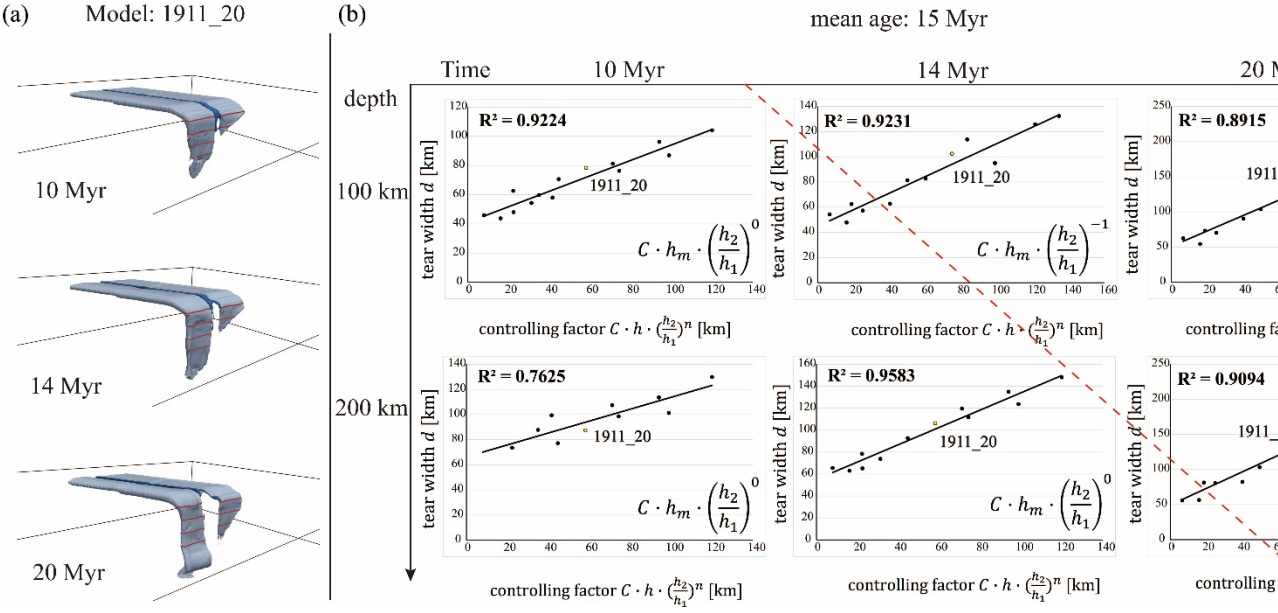

Figure 6. (a) Snapshots of particular model 1911_20 (slabs reference ages t1=19 Myr, t2=11 Myr, mean age 15 Myr, and subduction obliqueness θ=20°) at 10, 14, and 20 Myr of simulated time, showing the evolution of the slabs and the transform tearing. The red curves on slabs are selected paths for geometry and tearing assessment computation. (b) The six different panels display trials on the functional forms of $(C \bullet h \bullet (\frac{h_2}{h_1})^n)$ depending on evolution time (large horizontal axis) and depth (large vertical axis) and their correlation with the horizontal tearing width (d). The correlation coefficient (top left corner) between tearing horizontal width (small vertical axis) and velocity difference controlling factor (small horizontal axis) is shown on each panel's top-left corner. The variable range outlined by the dashed red line on the phase diagram corresponds to the model at the corresponding combinations. (c) The major force analysis of the tip part of a two-dimensional subducting slab with slab thickness h, initial slab length l, and subduction dip angle α. These plots illustrate the search for the maximum correlation coefficient between the slabs tear horizontal-width and the slab-segments velocity difference by varying different functional forms.

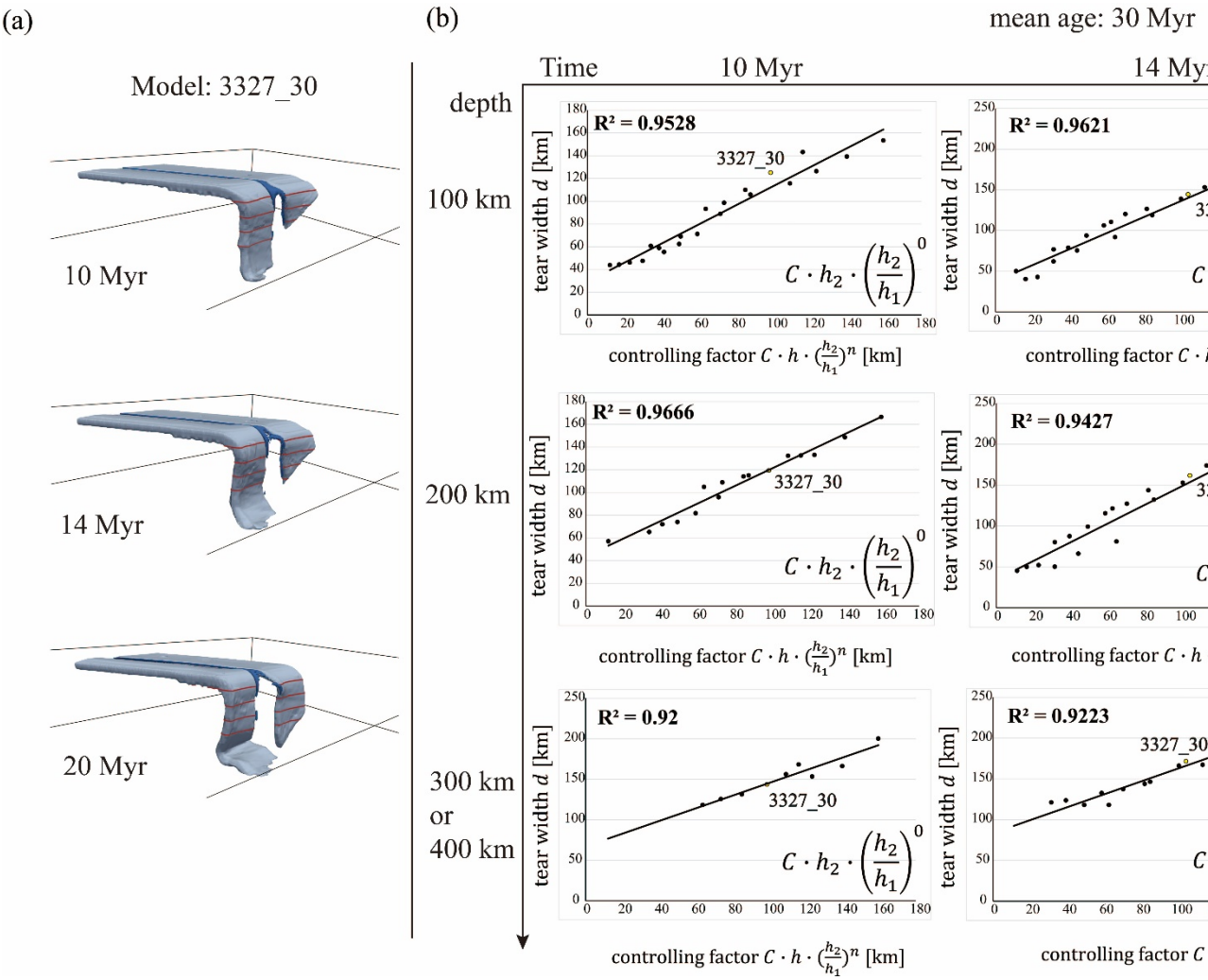

Figure 7. (a) Snapshots of particular model 3327_30 (slabs reference ages t1=33 Myr, t2=27 Myr, mean age 30 Myr, and subduction obliqueness θ=30°) at 10, 14, and 20 Myr, showing the evolution of the slab tearing. The red curves on slabs are selected slices for geometry and tearing assessment computation. (b) The nine different panels display the correlation between slab tearing horizontal width (d) and the integrated, controlling factor ($C \bullet h \bullet (\frac{h_2}{h_1})^n$). Correlation coefficients (R^2) are shown on the top-left corner of each panel.

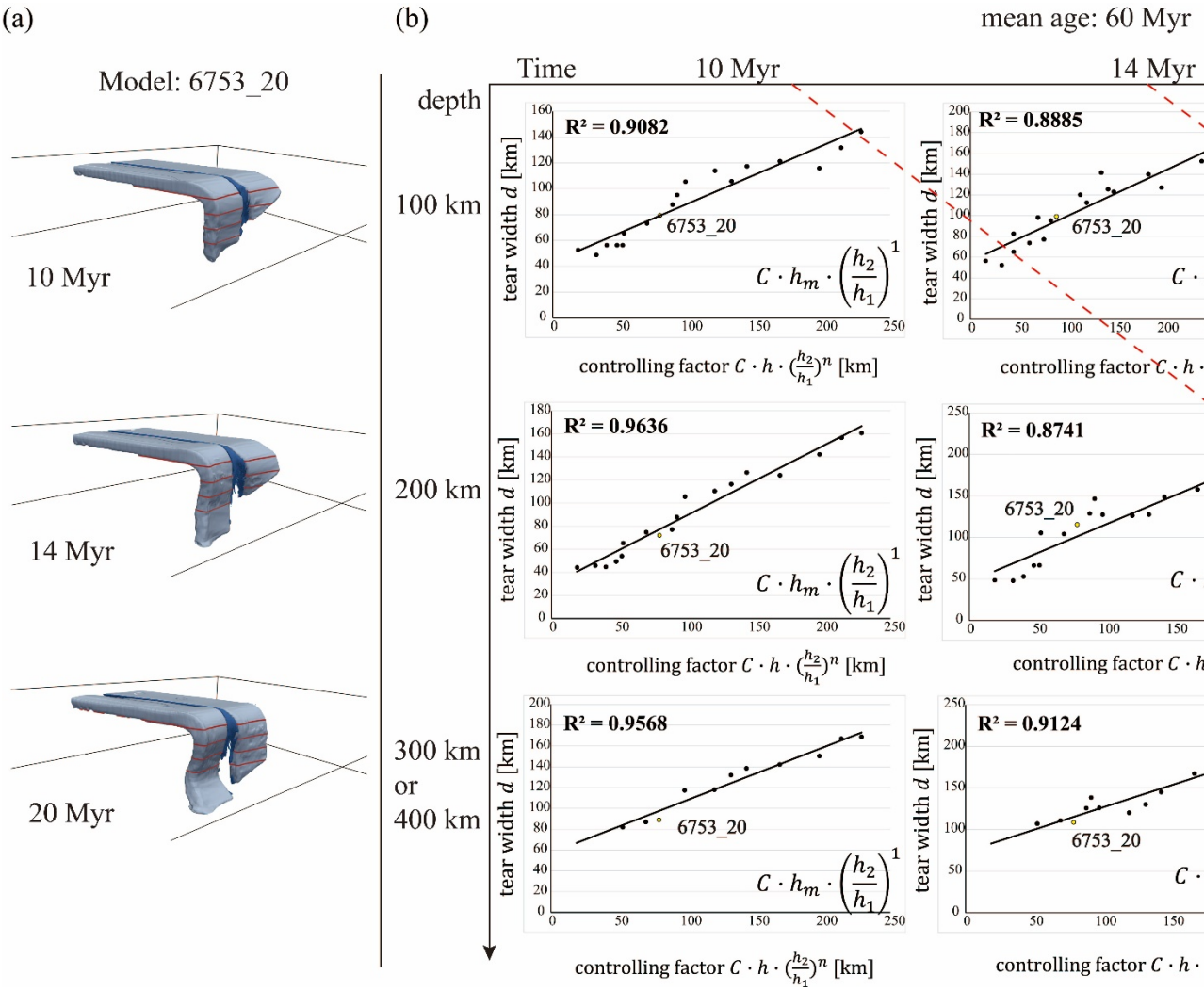

Figure 8. (a) Snapshots of particular model 6753_20 (slabs reference ages t1=67 Myr, t2=53 Myr, mean age 60 Myr, and subduction obliqueness θ=20°) at 10, 14, and 20 Myr, showing the evolution of the slab tearing. The red curves on slabs are selected slices for geometry and tearing assessment computation. (b) The nine different panels display the correlation between slab tearing horizontal width (d) and the integrated, controlling factor ($C \bullet h \bullet (\frac{h_2}{h_1})^n$). Correlation coefficients (R^2) are shown on the top-left corner of each panel.

After a detailed analysis of our numerical experiments (Figures 6-8), we find that the tearing horizontal width d is roughly proportional to a simple form of $C \bullet h \bullet (\frac{h_2}{h_1})^n$, with the correlation coefficient R^2 in the range of 0.76~0.97. In the simplest functional case " $v = k \bullet C$," the range of R^2 is 0.57~0.96 with respect

to different mean age groups (15, 30, 60 Myr) and all models (Table 3). The first-order governing factor is the oblique convergence characteristic parameter C, as defined in Equation 6.

Table 3. The correlation between the tearing horizontal width "d" and the oblique convergence characteristic parameter C (as constructing the simplest parametric function " $v = k \bullet C$") at different times and depths [a].

$R^2(d,\ v)$-15 Myr	10 Myr	14 Myr	20 Myr
100 km	0.92	0.85	0.81
200 km	0.76	0.96	0.84
300 km	——	——	——
400 km	——	——	——
$R^2(d,\ v)$-30 Myr	10 Myr	14 Myr	20 Myr
100 km	0.93	0.96	0.94
200 km	0.92	0.94	0.96
300 km	0.95	0.92	——
400 km	——	0.92	0.91
$R^2(d,\ v)$-60 Myr	10 Myr	14 Myr	20 Myr
100 km	0.83	0.90	0.83
200 km	0.86	0.84	0.88
300 km	0.87	0.87	——
400 km	——	0.92	0.89
$R^2(d,\ v)$-all	10 Myr	14 Myr	20 Myr
100 km	0.77	0.79	0.70
200 km	0.80	0.81	0.69
300 km	0.71	0.73	——
400 km	——	0.57	0.76

[a] The value range of C is 0.57~0.96.

In particular, if we divide each group of time-depth diagrams along the diagonal line (Figures 6-8), the parameter changes can roughly reflect the tearing width evolution in different segments of the ocean plate. The variation of parameters in various intervals from the lower left to the upper right depicts the variation of governing factors from the front edge to the back edge of the oceanic plate, which is dependent on $(\frac{h_2}{h_1})^n$ (n: 1→0→-1). This evolution simply represents the effect of unbending resistance F_2 in various plate segments. The slab length l of plate-2 is obviously smaller than that of plate-1 during the early stages of subduction (well before the two slabs are dipping sub-vertically). Accordingly, "stiffer" plate-2 affects the change of tearing width when $h = h_2, n = 1$. The overall subduction dip angle (including that of plate 1) increases as plate-2 subducts, and the effects of F_2 grow weaker at this point $h = h_{\text{mean}}, n = 0$.

Later on, with continued slabs sinking, there is the singular event of plate-1 reaching 660 km depth: Plate-1 is subjected to a force at the bottom that resists bending. At this point, the v turns to be controlled by plate-1, $n = -1$.

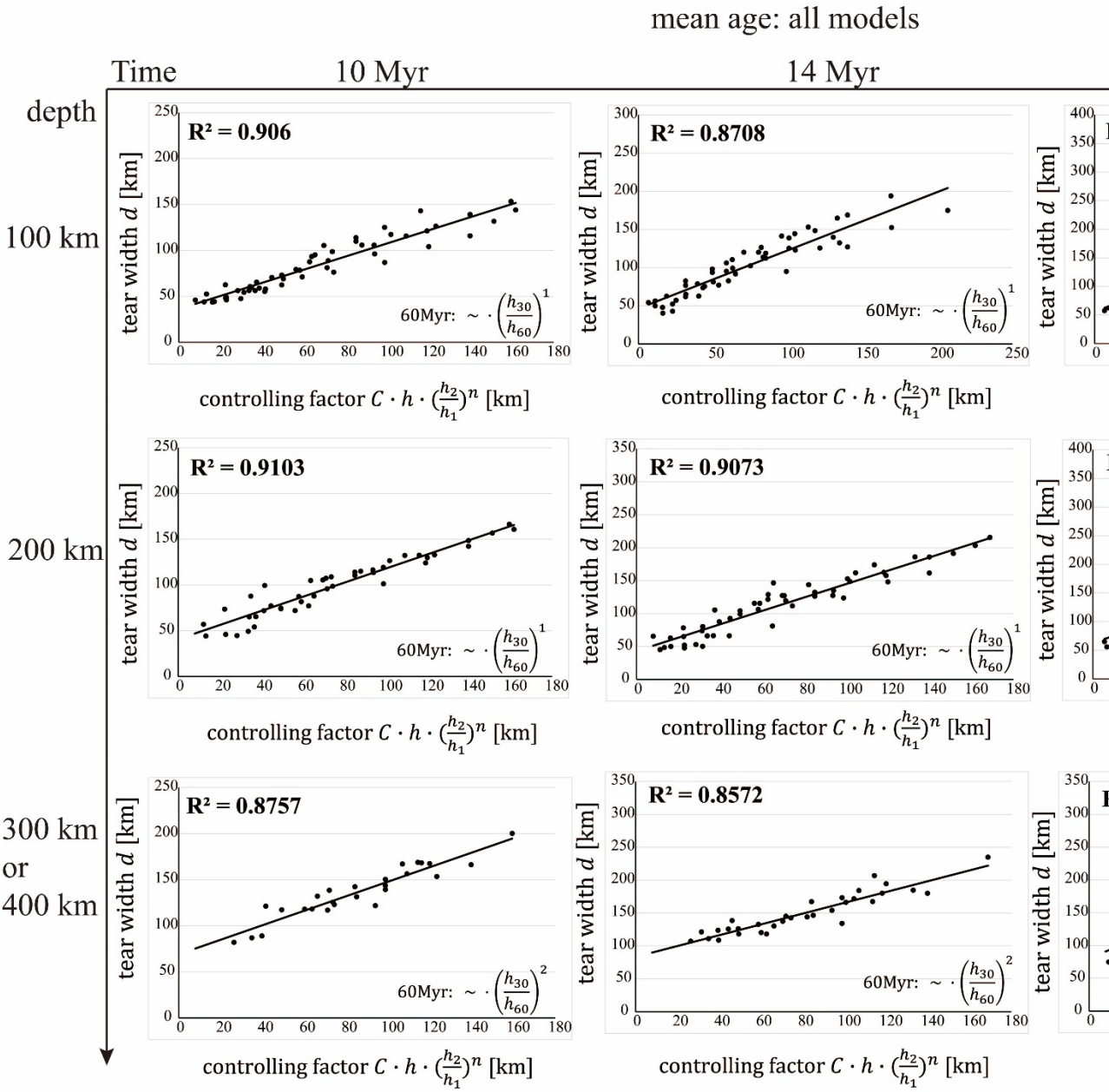

Figure 9. The nine different panels display the correlation between slab tearing width (d) and the integrated, controlling factor ($C \bullet h \bullet (\frac{h_2}{h_1})^n$) for all models.

The correlation coefficients (R^2) are shown on the top left corner of each panel. The red dashed line on the phase diagram corresponds to a regime transition. An additional multiplication factor $(\frac{h_{30}}{h_{60}})^p$ must be applied in the 60 Myr mean-age simulations to capture the influence of slab thickness variation on tearing width.

The comparison among the models with different mean slab ages indicates that the older slabs of 60 Myr generally have a narrower tearing window than the younger slabs with mean ages of 15 and 30 Myr. To measure the effect of bending length $\frac{l_{b1}}{l_{b2}}$, we use the average slab-thickness ratio $(\frac{h_{30Myr}}{h_{60Myr}})^p$, which can be compared quantitatively. It turns out that the 60 Myr group necessitates an additional multiplication term to maximize the correlation coefficient (R^2) (Figures 9). A possible explanation is that the sequence of plate-1,2 changing from small bending length to large bending length is different when plate thicknesses are large. The rheologically weaker plate-1 changes earlier in the plate-thickness sinking-velocity parameter space than plate-2, increasing the tearing width from 15 Myr-age groups to 30 Myr-age groups and then decreasing from 30 Myr-age groups to 60 Myr-age groups. This effect is more apparent in the later phases of subduction and at larger depths, as shown by the change of p in Figure 9. This feature is also shown in the shift of the age ratio cut-off with absolute age in Figure 4.

In summary, vertical slab tearing is controlled by two dominant factors, (i) the subduction horizontal obliqueness: the larger the obliqueness angle, the higher the likelihood for slab tearing; (ii) the slab-transform age difference: slab tearing is favored by older, heavier, thicker plate-1 relative to plate-2. The plates' unbending resistance effect varies among subduction zones and has a secondary role in tearing generation and development.

4.2. Geological application

As shown in Figure 10, examples of slab tearing of natural subduction zones are projected onto our simulations' phase diagrams. Some cases (such as "cam-1" and "ala") are shown in two mean-age groups, given our sparse sampling of this variable. Except for the "ala" point, all the natural cases fall in the regime where tearing occurs. The misfit of the "ala" case may be due to a secondary plate with different seafloor ages (Yang & Gao, 2020). Furthermore, because the obliqueness angle of "car" and "ker" is 60°, we have not carried out corresponding simulations considering the numerical stability problems they face. The Aleutian slab window's low-velocity zone emplaced on a high oblique-convergence angle may undergo tearing as an effect of plate-1 bending enforced by the overriding plate (Bai et al., 2020). However, the former exhibits a strong seafloor age contrast, with plate-2 being older and thicker (more prone to sinking). Thus, the slab-ages combination likely exerts an opposite effect on the tearing development, probably decreasing or slowing down the tearing width.

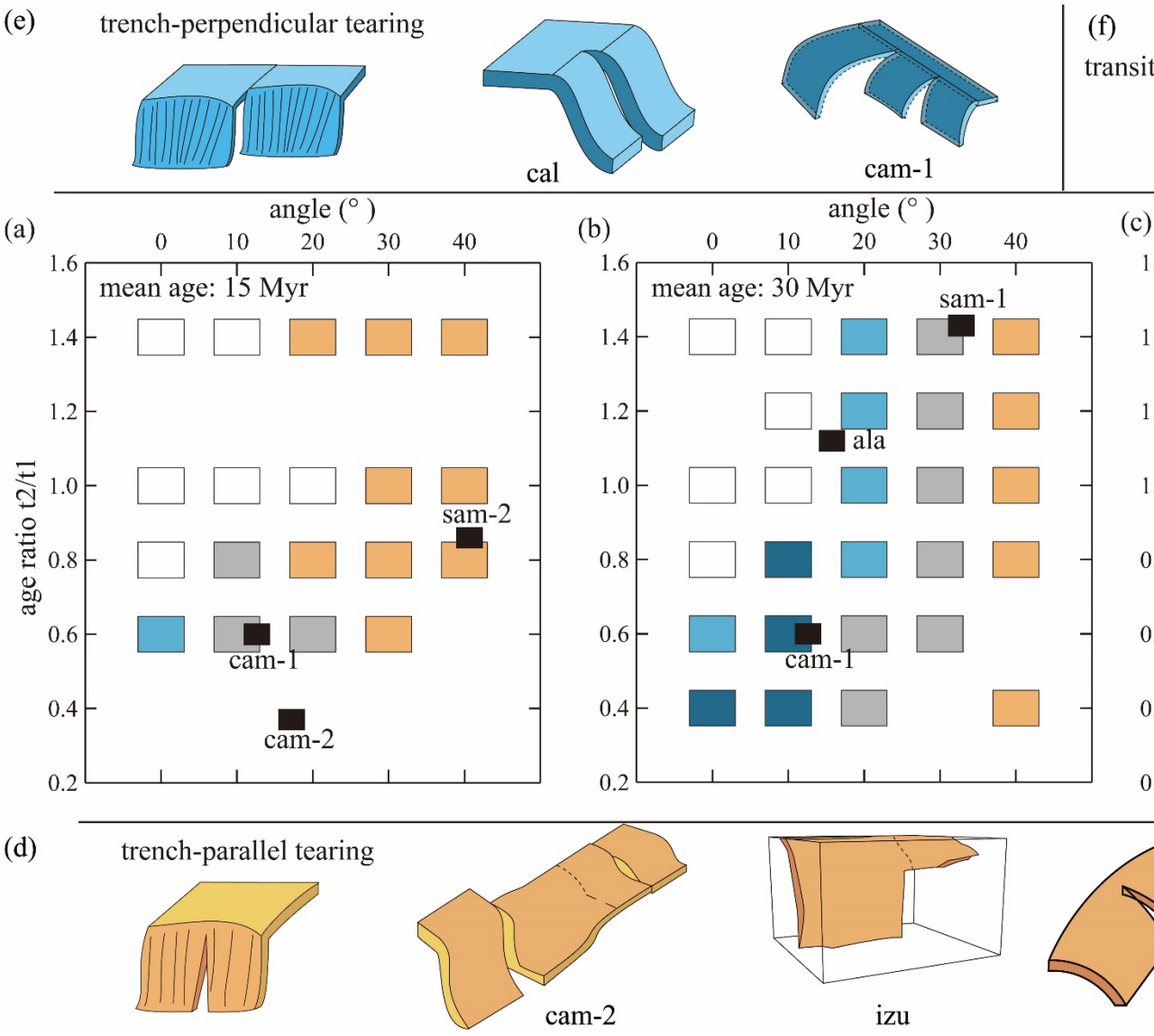

Figure 10. Comparisons between numerical model predictions (tearing pattern phase diagrams with color rectangles) and subduction-zones observations (small black rectangles) along with their simplified observation-based interpreted structures (cartoons). All the natural cases are consistent with the numerical prediction, except for the Alaska case "**ala**" and the northwestern South America case "**sam-2**". The "**ala**" natural case falling in the predicted no-tearing zone may be affected by a secondary, so far unobserved, slab tear in nature. In contrast, the "**sam-2** differential retreat" case in the trench-parallel pattern zone may be affected by a lateral break off in the younger slab but also lack

more detailed local observations.

We discovered or conceptualized trench-parallel tearing, which is revealed or suggested by "cam-2", "Izu," and "car" in the expanded region of the phase diagram. Aside from that, we confirmed the well-known trench-perpendicular tearing, which is revealed by "cal," "cam-1". The "sam-1" is in the transitional mode's zone with both features.

The simulations do not fit the real "sam-2" tearing pattern, most likely due to the real plate being too thin and experiencing break-off in a differential roll back style, as shown in Figure 1 and Table 1, yet inconsistently falling within our trench-parallel tearing combinations. According to our understanding, the vertical tearing patterns of Tonga "ker" and Caribbean "car" correspond to transitional mode (trench-parallel evolving to trench-perpendicular), and Kamchatka "kam" tends to trench-perpendicular tearing.

Imaging (mostly seismic) findings of "cam-1", "sam-1", and "Izu" show the feature of varied subduction depths (slab tips) on both sides of the transform fault. However, it is unclear how compatible that is with our model setup assumption about initial plate emplacement (with variability along strike). Finally, when plate-2 is not entirely subducted during the early stages of subduction evolution, the varied slab length l along the trench generates transverse non-uniform slab "stiffness" (Li & Ribe, 2012). (Obviously, the smaller l, the stronger the unbending resistance and the stiffer the slab). This phenomenon should be somewhat reflected in the continuous variation in subduction dip angle along the trench of the right (northern) slab in the "sam-1" cartoon (Figure 10).

4.3. Model limitations

Our model is simplified by having constant (yet adequate) density, viscosity, and thermal properties values. It is chosen to isolate the first-order controls on the slab tearing during transform fault subduction. This simplification may lead to some inaccuracies, such as:

(1) The age difference between the two sides of the transform fault should lead to additional lateral variations in the physical properties (e.g. viscosities) of the oceanic plate.

(2) The viscosity and density should vary continuously with depth (pressure and temperature), particularly through and between lithospheric and asthenospheric mantle regions.

(3) Additional complexities and different effects on the sinking-tearing plate, i.e., more specific and refined forms of the function f, which were not tried.

(4) The obliqueness angle and age ratio data for the natural cases of the early stages of subduction may be slightly different from the present day.

All the aforementioned neglected factors can influence the exact magnitude of tearing at all stages during subduction. However, we believe that the first-order controlling mechanisms are adequately represented in our study.

5. Conclusions

Subduction horizontal obliqueness and slab transform age difference both play dominant first-order roles in the development and evolution of tearing during subduction of such complex systems. The plates' unbending resistance, which varies among subduction zones, seems to have a secondary role in slab tearing.

When the subduction horizontal-obliqueness angle is 30° or the age ratio of plate-2 to plate-1 is less than 0.6, fast and well-developed slab vertical tearing occurs and develops inside the mantle without any other requirements. In contrast, no tearing occurs for small obliqueness angles (<20°) if the plate-2 is approximately older and thicker (age ratio >0.6-0.8).

Slab tearing can occur in two different patterns or modes when referred to the trench orientation: trench-parallel and trench-perpendicular tearing. Trench-parallel tearing manifests for medium-high subduction horizontal-obliqueness angles (>20°) if and only if the slabs' mean age is <60 Myr. Trench-perpendicular tearing (related to differential slabs-hinge retreat or rollback) manifests for certain combinations of medium-small obliqueness (<30°) angles and favorably low age ratios (i.e., thicker plate subducting first).

Our modeling suggests that the continual spatial variation in dip angle along the trench observed in real-Earth subduction zones could be potentially related to subducting slab's initial evolution under horizontally-oblique convergence and perhaps to slab tearing development inside the mantle. Further beyond, knowing the age combination across a transform fault (ratio and average) and the horizontal obliqueness of an oceanic subduction scenario would, with a framework like the one here presented, allow a prediction of the tearing occurrence, potential pattern and the likely evolution, and thus of the associated locally-perturbed mantle flow.

Acknowledgments

We appreciate Dr. Yimin Jin's great help in troubleshooting-running the ASPECT program. This research is supported by the National Natural Science Foundation of China (41725017), the National Key R&D Program of the Ministry of Science and Technology of China (2020YFA0713400), and the Strategic Priority Research Program (B) of the Chinese Academy of Sciences (XDB18010202).

The original datasets are published as a Zenodo data package (https://zenodo.org/record/7066493#.Yx27fnZByUk) . The numerical software ASPECT is from https://aspect.geodynamics.org/ and visualization software ParaView is https://www.paraview.org/. Figure 1 is plotted with GMT https://www.generic-mapping-tools.org/ , and the original data on the subduction zone, seafloor age, plate velocity and color bar are referred to (Hayes et al., 2018b), (Müller et al., 2008), (Becker et al., 2015), and (Crameri, 2021), respectively.

References

Bai, Y., Zhang, D., Dong, D., Wu, S., & Wang, Z. (2020). Aleutian island arc magma production rates and primary controlling factors. *Marine Geology*, *430*, 106346. https://doi.org/10.1016/j.margeo.2020.106346Bangerth, W., Dannberg, J., Fraters, M., Gassmoeller, R., Glerum, A., Heister, T., & Naliboff, J. (2021). *ASPECT v2.3.0*. Zenodo. https://doi.org/10.5281/zenodo.5131909Becker, T. W., Schaeffer, A. J., Lebedev, S., & Conrad, C. P. (2015). Toward a generalized plate motion reference frame. *Geophysical Research Letters*, *42*(9), 3188–3196. https://doi.org/10.1002/2015GL063695Bolton, A. R., Schutt, D. L., Aster, R. C., Audet, P., Schaeffer, A. J., Estève, C., et al. (2022). Evidence for asthenospheric flow rotation in northwest Canada: insights from shear wave splitting. *Geophysical Journal International*, *228*(3), 1780–1792. https://doi.org/10.1093/gji/ggab396Bonnardot, M.-A., Régnier, M., Christova, C., Ruellan, E., & Tric, E. (2009). Seismological evidence for a slab detachment in the Tonga subduction zone. *Tectonophysics*, *464*(1), 84–99. https://doi.org/10.1016/j.tecto.2008.10.011Burkett, E. R., & Billen, M. I. (2010). Three-dimensionality of slab detachment due to ridge-trench collision: Laterally simultaneous boudinage versus tear propagation. *Geochemistry, Geophysics, Geosystems*, *11*(11). https://doi.org/10.1029/2010GC003286Carciumaru, D., Ortega, R., Castellanos, J. C., & Huesca-Pérez, E. (2020). Crustal Characteristics in the Subduction Zone of Mexico: Implication of the Tectonostratigraphic Terranes on Slab Tearing. *Seismological Research Letters*, *91*(3), 1781–1793. https://doi.org/10.1785/0220190117Crameri, F. (2021). *Scientific colour maps*. Zenodo. https://doi.org/10.5281/zenodo.5501399Cui, Q., & Li, Z.-H. (2022). Along-Strike Variation of Convergence Rate and Pre-Existing Weakness Contribute to Indian Slab Tearing Beneath Tibetan Plateau. *Geophysical Research Letters*, *49*(4), e2022GL098019. https://doi.org/10.1029/2022GL098019Dougherty, S. L., & Clayton, R. W. (2014). Seismicity and structure in central Mexico: Evidence for a possible slab tear in the South Cocos plate. *Journal of Geophysical Research: Solid Earth*, *119*(4), 3424–3447. https://doi.org/10.1002/2013JB010883Duretz, T., Gerya, T. V., & May, D. A. (2011). Numerical modelling of spontaneous slab breakoff and subsequent topographic response. *Tectonophysics*, *502*(1), 244–256. https://doi.org/10.1016/j.tecto.2010.05.024Fernández-García, C., Guillaume, B., & Brun, J.-P. (2019). 3D slab breakoff in laboratory experiments. *Tectonophysics*, *773*, 228223. https://doi.org/10.1016/j.tecto.2019.228223Freeburn, R., Bouilhol, P., Maunder, B., Magni, V., & van Hunen, J. (2017). Numerical models of the magmatic processes induced by slab breakoff. *Earth and Planetary Science Letters*, *478*, 203–213. https://doi.org/10.1016/j.epsl.2017.09.008Georgieva, V., Melnick, D., Schildgen, T. F., Ehlers, T. A., Lagabrielle, Y., Enkelmann, E., & Strecker, M. R. (2016). Tectonic control on rock uplift, exhumation, and topography above an oceanic ridge collision: Southern Patagonian Andes (47°S), Chile. *Tectonics*, *35*(6), 1317–1341. https://doi.org/10.1002/2016TC004120Gerya, T. (2022). Numerical modeling of subduction: State of the art and future directions. *Geosphere*, *18*(2), 503–561. https://doi.org/10.1130/GES02416.1Gianni, G. M., & Luján, S. P. (2021). Geodynamic controls on magmatic

arc migration and quiescence. *Earth-Science Reviews*, *218*, 103676. https://doi.org/10.1016/j.earscirev.2021.103676Gianni, G. M., Navarrete, C., & Spagnotto, S. (2019). Surface and mantle records reveal an ancient slab tear beneath Gondwana. *Scientific Reports*, *9*(1), 19774. https://doi.org/10.1038/s41598-019-56335-9Glerum, A., Thieulot, C., Fraters, M., Blom, C., & Spakman, W. (2018). Nonlinear viscoplasticity in ASPECT: benchmarking and applications to subduction. *Solid Earth*, *9*(2), 267–294. https://doi.org/10.5194/se-9-267-2018Govers, R., & Wortel, M. J. R. (2005). Lithosphere tearing at STEP faults: response to edges of subduction zones. *Earth and Planetary Science Letters*, *236*(1), 505–523. https://doi.org/10.1016/j.epsl.2005.03.022Govers, Rob, & Fichtner, A. (2016). Signature of slab fragmentation beneath Anatolia from full-waveform tomography. *Earth and Planetary Science Letters*, *450*, 10–19. https://doi.org/10.1016/j.epsl.2016.06.014Guillaume, B., Moroni, M., Funiciello, F., Martinod, J., & Faccenna, C. (2010). Mantle flow and dynamic topography associated with slab window opening: Insights from laboratory models. *Tectonophysics*, *496*(1), 83–98. https://doi.org/10.1016/j.tecto.2010.10.014Hayes, G. P., Moore, G. L., Portner, D. E., Hearne, M., Flamme, H., Furtney, M., & Smoczyk, G. M. (2018a). Slab2, a comprehensive subduction zone geometry model. *Science*. https://doi.org/10.1126/science.aat4723Hayes, G. P., Moore, G. L., Portner, D. E., Hearne, M., Flamme, H., Furtney, M., & Smoczyk, G. M. (2018b). Slab2, a comprehensive subduction zone geometry model. *Science*. https://doi.org/10.1126/science.aat4723Hildebrand, R. S., Whalen, J. B., & Bowring, S. A. (2018). Resolving the crustal composition paradox by 3.8 billion years of slab failure magmatism and collisional recycling of continental crust. *Tectonophysics*, *734–735*, 69–88. https://doi.org/10.1016/j.tecto.2018.04.001Jolivet, L., Menant, A., Sternai, P., Rabillard, A., Arbaret, L., Augier, R., et al. (2015). The geological signature of a slab tear below the Aegean. *Tectonophysics*, *659*, 166–182. https://doi.org/10.1016/j.tecto.2015.08.004Jolivet, L., Menant, A., Roche, V., Pourhiet, L. L., Maillard, A., Augier, R., et al. (2021). Transfer zones in Mediterranean back-arc regions and tear faults. *BSGF - Earth Sciences Bulletin*, *192*, 11. https://doi.org/10.1051/bsgf/2021006Király, Á., Portner, D. E., Haynie, K. L., Chilson-Parks, B. H., Ghosh, T., Jadamec, M., et al. (2020). The effect of slab gaps on subduction dynamics and mantle upwelling. *Tectonophysics*, *785*, 228458. https://doi.org/10.1016/j.tecto.2020.228458Kufner, S.-K., Schurr, B., Haberland, C., Zhang, Y., Saul, J., Ischuk, A., & Oimahmadov, I. (2017). Zooming into the Hindu Kush slab break-off: A rare glimpse on the terminal stage of subduction. *Earth and Planetary Science Letters*, *461*, 127–140. https://doi.org/10.1016/j.epsl.2016.12.043Levin, V., Shapiro, N., Park, J., & Ritzwoller, M. (2002). Seismic evidence for catastrophic slab loss beneath Kamchatka. *Nature*, *418*(6899), 763–767. https://doi.org/10.1038/nature00973Li, Z.-H., & Ribe, N. M. (2012). Dynamics of free subduction from 3-D boundary element modeling. *Journal of Geophysical Research: Solid Earth*, *117*(B6). https://doi.org/10.1029/2012JB009165Li,

Z.-H., Xu, Z., Gerya, T., & Burg, J.-P. (2013). Collision of continental corner from 3-D numerical modeling. *Earth and Planetary Science Letters*, *380*, 98–111. https://doi.org/10.1016/j.epsl.2013.08.034Liu, K., Zhang, J., Xiao, W., Wilde, S. A., & Alexandrov, I. (2020). A review of magmatism and deformation history along the NE Asian margin from ca. 95 to 30 Ma: Transition from the Izanagi to Pacific plate subduction in the early Cenozoic. *Earth-Science Reviews*, *209*, 103317. https://doi.org/10.1016/j.earscirev.2020.103317Liu, L., Liu, L., & Xu, Y.-G. (2021). Mesozoic intraplate tectonism of East Asia due to flat subduction of a composite terrane slab. *Earth-Science Reviews*, *214*, 103505. https://doi.org/10.1016/j.earscirev.2021.103505Magni, V., Faccenna, C., van Hunen, J., & Funiciello, F. (2014). How collision triggers backarc extension: Insight into Mediterranean style of extension from 3-D numerical models. *Geology*, *42*(6), 511–514. https://doi.org/10.1130/G35446.1Meighan, H. E., Pulliam, J., Brink, U. ten, & López-Venegas, A. M. (2013). Seismic evidence for a slab tear at the Puerto Rico Trench. *Journal of Geophysical Research: Solid Earth*, *118*(6), 2915–2923. https://doi.org/10.1002/jgrb.50227Millen, D. W., & Hamburger, M. W. (1998). Seismological evidence for tearing of the Pacific plate at the northern termination of the Tonga subduction zone. *Geology*, *26*(7), 659–662. https://doi.org/10.1130/0091-7613(1998)026<0659:SEFTOT>2.3.CO;2Miller, M. S., Kennett, B. L. N., & Lister, G. S. (2004). Imaging changes in morphology, geometry, and physical properties of the subducting Pacific plate along the Izu–Bonin–Mariana arc. *Earth and Planetary Science Letters*, *224*(3), 363–370. https://doi.org/10.1016/j.epsl.2004.05.018Miller, Meghan S., Gorbatov, A., & Kennett, B. L. N. (2006). Three-dimensional visualization of a near-vertical slab tear beneath the southern Mariana arc. *Geochemistry, Geophysics, Geosystems*, *7*(6). https://doi.org/10.1029/2005GC001110Müller, R. D., Sdrolias, M., Gaina, C., & Roest, W. R. (2008). Age, spreading rates, and spreading asymmetry of the world's ocean crust. *Geochemistry, Geophysics, Geosystems*, *9*(4). https://doi.org/10.1029/2007GC001743Pesicek, J. D., Engdahl, E. R., Thurber, C. H., DeShon, H. R., & Lange, D. (2012). Mantle subducting slab structure in the region of the 2010 M8.8 Maule earthquake (30–40°S), Chile. *Geophysical Journal International*, *191*(1), 317–324. https://doi.org/10.1111/j.1365-246X.2012.05624.xPusok, A. E., Kaus, B. J. P., & Popov, A. A. (2018). The effect of rheological approximations in 3-D numerical simulations of subduction and collision. *Tectonophysics*, *746*, 296–311. https://doi.org/10.1016/j.tecto.2018.04.017Ribe, N. M. (2001). Bending and stretching of thin viscous sheets. *Journal of Fluid Mechanics*, *433*, 135–160. https://doi.org/10.1017/S0022112000003360Roche, V., Sternai, P., Guillou-Frottier, L., Menant, A., Jolivet, L., Bouchot, V., & Gerya, T. (2018). Emplacement of metamorphic core complexes and associated geothermal systems controlled by slab dynamics. *Earth and Planetary Science Letters*, *498*, 322–333. https://doi.org/10.1016/j.epsl.2018.06.043Rosenbaum, G., Gasparon, M., Lucente, F. P., Peccerillo, A., & Miller, M. S. (2008). Kinematics of slab tear faults during subduction segmentation and implications for Italian magmatism. *Tectonics*, *27*(2). https://doi.org/10.1029/2007TC002143Stubailo, I., Beghein, C., & Davis, P. M. (2012). Structure and anisotropy of the Mexico

subduction zone based on Rayleigh-wave analysis and implications for the geometry of the Trans-Mexican Volcanic Belt. *Journal of Geophysical Research: Solid Earth*, *117*(B5). https://doi.org/10.1029/2011JB008631Suckale, J., Rondenay, S., Sachpazi, M., Charalampakis, M., Hosa, A., & Royden, L. H. (2009). High-resolution seismic imaging of the western Hellenic subduction zone using teleseismic scattered waves. *Geophysical Journal International*, *178*(2), 775–791. https://doi.org/10.1111/j.1365-246X.2009.04170.xThorkelson, D. J. (1996). Subduction of diverging plates and the principles of slab window formation. *Tectonophysics*, *255*(1), 47–63. https://doi.org/10.1016/0040-1951(95)00106-9Turcotte, D. L., & Schubert, G. (2002). *Geodynamics* (2nd ed.). Cambridge University Press. https://doi.org/10.1017/CBO9780511807442Vargas, C. A., & Mann, P. (2013). Tearing and Breaking Off of Subducted Slabs as the Result of Collision of the Panama Arc-Indenter with Northwestern South America. *Bulletin of the Seismological Society of America*, *103*(3), 2025–2046. https://doi.org/10.1785/0120120328Xu, Y., Wang, Q., Tang, G., Wang, J., Li, H., Zhou, J., et al. (2020). The origin of arc basalts: New advances and remaining questions. *Science China Earth Sciences*, *63*(12), 1969–1991. https://doi.org/10.1007/s11430-020-9675-yYang, X., & Gao, H. (2020). Segmentation of the Aleutian-Alaska Subduction Zone Revealed by Full-Wave Ambient Noise Tomography: Implications for the Along-Strike Variation of Volcanism. *Journal of Geophysical Research: Solid Earth*, *125*(11), e2020JB019677. https://doi.org/10.1029/2020JB019677